GOCE: The first seismometer in orbit around the Earth

Raphael Garcia, Sean Bruinsma, Philippe Lognonné, Eelco N Doornbos, Florian Cachoux

▶ **To cite this version:**

Raphael Garcia, Sean Bruinsma, Philippe Lognonné, Eelco N Doornbos, Florian Cachoux. GOCE: The first seismometer in orbit around the Earth. Geophysical Research Letters, 2013, 40 (5), pp.1015-1020. 10.1002/grl.50205 . insu-02563854

HAL Id: insu-02563854
https://insu.hal.science/insu-02563854

Submitted on 6 Aug 2020

HAL is a multi-disciplinary open access archive for the deposit and dissemination of scientific research documents, whether they are published or not. The documents may come from teaching and research institutions in France or abroad, or from public or private research centers.

L'archive ouverte pluridisciplinaire **HAL**, est destinée au dépôt et à la diffusion de documents scientifiques de niveau recherche, publiés ou non, émanant des établissements d'enseignement et de recherche français ou étrangers, des laboratoires publics ou privés.

GOCE: The first seismometer in orbit around the Earth

Raphael F. Garcia,[1,2] Sean Bruinsma,[3] Philippe Lognonné,[4] Eelco Doornbos,[5] and Florian Cachoux[1,6]

Received 3 December 2012; revised 25 January 2013; accepted 25 January 2013; published 14 March 2013.

[1] The first in situ sounding of a post-seismic infrasound wavefront is presented, using data from the GOCE mission. The atmospheric infrasounds following the great Tohoku earthquake (on 11 March 2011) induce variations of air density and vertical acceleration of the GOCE platform. These signals are detected at two positions along the GOCE orbit corresponding to a crossing and a doubling of the infrasonic wavefront created by seismic surface waves. Perturbations up to 11% of air density and 1.35×10^{-7} m/s^2 of vertical acceleration are observed and modeled with two different solid-atmosphere coupling codes. These perturbations are a due to acoustic waves creating vertical velocities up to 130 m/s. Amplitudes and arrival times of these perturbations are reproduced respectively within a factor 2, and within a 60 s time window. Waveforms present a good agreement with observed data. The vertical acceleration to air density perturbation ratio is higher for these acoustic waves than for gravity waves. Combining these two pieces of information offers a new way to distinguish between these two wave types. This new type of data is a benchmark for the models of solid-atmosphere coupling. Amplitude and frequency content constrain the infrasound attenuation related to atmosphere viscosity and thermal conductivity. Observed time shifts between data and synthetics are ascribed to lateral variations of the seismic and atmospheric sound velocities and to the influence of atmospheric winds. These effects should be included in future modeling. This validation of our modeling tools allows to specify more precisely future observation projects. **Citation:** Garcia, R. F., S. Bruinsma, P. Lognonné, E. Doornbos, and F. Cachoux (2013), GOCE: the first seismometer in orbit around the Earth, *Geophys. Res. Lett.*, *40*, 1015–1020, doi:10.1002/grl.50205.

1. Introduction

[2] Mechanical coupling between solid Earth, ocean, and atmosphere induces propagation of acoustic waves in the atmosphere following earthquakes and gravity waves following tsunamis. During their vertical propagation, these waves are amplified because of the decreasing atmospheric density and attenuated because of energy losses due to thermal and mechanical diffusion. Theoretical simulations of the solid-atmosphere coupling began with simulation of gravity waves generated by tsunamis [*Hines*, 1960]. The most complete description of the acoustic wave coupling up to now is based on the computation of "full Earth" normal modes including atmosphere and attenuation processes [*Lognonné et al.*, 1998; *Artru et al.*, 2001]. The atmospheric waves are expected to have a maximum amplitude in the 200–350 km altitude range, depending on the frequency and on atmospheric properties, and are dissipated at higher altitudes. The associated leaky normal modes can be computed either by variational methods [*Lognonné et al.*, 1998] or propagators [*Kobayashi*, 2007; *Watada and Kanamori*, 2010] and the seismograms computed by normal mode summations [*Artru et al.*, 2004; *Rolland et al.*, 2011a].

[3] To date, most of the thermospheric observations of waves generated by seismic waves and tsunamis, following the Tohoku 11 March 2011 Mw = 9 quake, have sensed the ionospheric electron perturbations induced by neutral density waves. Electron vertical velocities were measured by ionospheric radars [*Nishitani et al.*, 2011] and doppler sounders [*Chum et al.*, 2012], while electron density perturbations were detected by ionosonds [*Maruyama et al.*, 2011] or global positioning systems [*Rolland et al.*, 2011b]. For the first time, airglow modulation of the tsunami waves was also detected [*Makela et al.*, 2011] enabling the generation of movies showing the tsunami propagation.

[4] However, all these observations rely on indirect measurements of the acoustic or gravity waves propagating in the neutral atmosphere. Because the dynamics of the electrons is different from the neutrals in the ionosphere [*Kherani et al.*, 2009], the electron density perturbations are influenced by many factors, the most important being the local magnetic field [*Dautermann et al.*, 2009]. As a consequence, the estimate of neutral wave amplitude and propagation properties from electron density perturbations is a complex process [*Occhipinti et al.*, 2011; *Kherani et al.*, 2012; *Galvan et al.*, 2012]. In particular, the recovery of the neutral wave field from these data is non-unique, because the electron density is mainly influenced by the neutral wave velocity along magnetic field lines.

[5] So far, observation of the Tohoku neutral waves has been limited to the detection of gravito-acoustic waves with micro-barometers [*Arai et al.*, 2011; *Raveloson et al.*, 2012]. We present here the first direct observation of post-seismic neutral acoustic waves in the thermosphere, along the GOCE orbit. The very low Earth orbit of the GOCE mission, at 270 km altitude, its drag compensated platform, and the unprecedented quality of its accelerometers [*Floberghagen*

[1]Université de Toulouse, UPS-OMP; IRAP, Toulouse, France
[2]CNRS, IRAP, Toulouse, France
[3]CNES, Department of Terrestrial and Planetary Geodesy, Toulouse, France
[4]Univ. Paris Diderot, Sorbonne Paris Cité, Institut de Physique du Globe de Paris, UMR 7154 CNRS, Paris, France
[5]Faculty of Aerospace Engineering, TU Delft, Delft, Netherlands
[6]EOST, Strasbourg, France

Corresponding author: R. F. Garcia, Institut de Recherche en Astrophysique et Planétologie, Observatoire Midi-Pyrénées, Université de Toulouse Paul Sabatier, 14 avenue E. Belin, 31400 Toulouse, France. (rgarcia@irap.omp.eu)

©2013. American Geophysical Union. All Rights Reserved.
0094-8276/13/10.1002/grl.50205

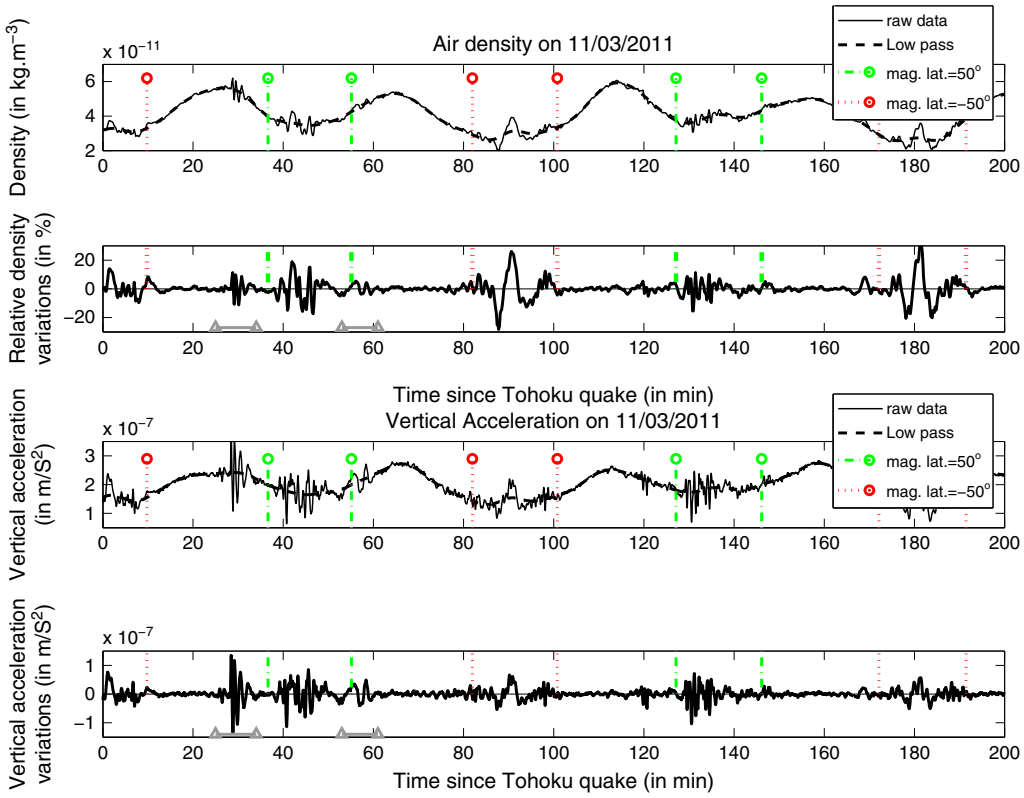

Figure 1. From top to bottom, raw air density data (in kg/m^3), relative air density variations (in %), raw GOCE vertical acceleration (in m/s^2), and vertical acceleration perturbations (in m/s^2) as a function of time (in minutes after the quake) along the GOCE orbit. The perturbations are obtained by subtracting the low-passed signal from the raw data. Time windows corresponding to perturbations ascribed to post-seismic infrasounds are indicated by gray lines. Data in between two dashed (or dot-dashed) lines are excluded because they are acquired in the polar areas.

et al., 2011] allowed us to recover very precisely the non-gravitational forces exerted on the satellite. Among these forces, the ones due to density variations and vertical displacements created by post-seismic infrasounds are observed, in a similar way as atmospheric gravity waves [*Bruinsma and Fedrizzi*, 2012].

[6] Then we perform the modeling of these waves and compare their amplitude, timing, and waveshape to density and vertical acceleration variations observed by GOCE. Differences between observed and modeled signals and the investigations performed on other gravimetric satellite data sets are discussed. Finally, we conclude with a summary of the results and a perspective in term of future satellite mission designs and numerical modeling of these waves.

2. Post-Seismic Perturbations Observed by GOCE

[7] GOCE is designed to measure gravity variations using a gradiometer within a drag compensated platform [*Drinkwater et al.*, 2003]. This study will use two by-products of the mission measurements: the vertical acceleration of the satellite and the air density deduced from the drag compensation along the satellite track. The non-gravitational radial acceleration is deduced from the average of the two vertical accelerometers within the gradiometer. Its variations track the forces exerted by vertical winds along the satellite track. The vertical acceleration of the satellite is known to within 2*10^{-12} m/s^2 [*Floberghagen et al.*, 2011]. The air density is deduced from the analysis of thruster data compensating satellite drag and accelerometer measurements [*Doornbos et al.*, 2010]. Relative density background variations along the satellite track vary by about 1%. Non-gravitational accelerations in horizontal directions are not considered because these are implicitly included in the computation of air density.

[8] Figure 1 presents the variations of vertical acceleration and air density along the GOCE orbit just after the magnitude 9.1 Tohoku earthquake in Japan (5:46:23 UT on 11 March 2011). A clear periodicity is observed in the variations of these two parameters due to the orbit of the satellite. These long period variations are removed by high-pass filtering the original data. Perturbations due to polar thermosphere dynamics are also clearly visible for geomagnetic latitudes larger than 50° [*Bruinsma and Fedrizzi*, 2012]. Therefore, polar regions are excluded from our analysis. A clear high-frequency signal of 1.3×10^{-7} m/s^2 and 11% amplitude is observed, respectively, in the vertical acceleration and air density about 27 min after the quake before entering into the polar area. A low-frequency perturbation with half the amplitude of the first one is also observed about 56 min after the quake when the satellite goes out of the polar region. In order to interpret these signals in terms of post-seismic infrasounds, a full modeling taking into account the observation geometry is presented in the next section.

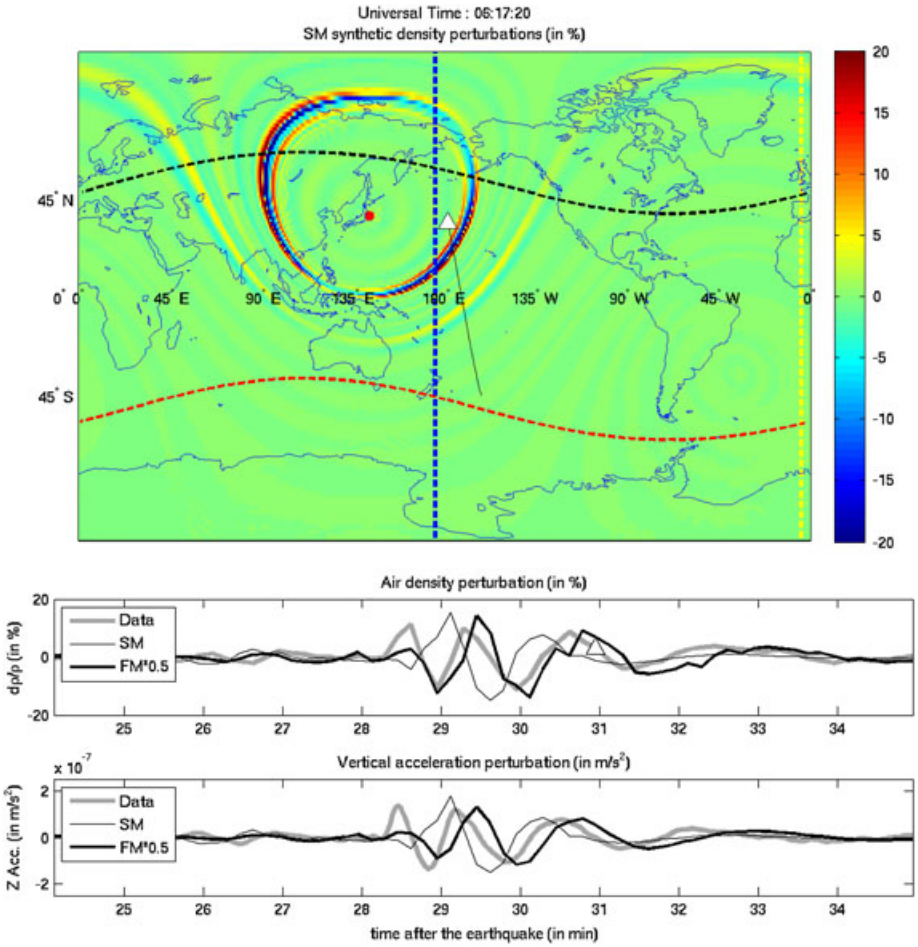

Figure 2. The upper panel presents a simple simulation (SM) of density perturbations (in %) at the altitude of GOCE and the satellite track around the first crossing of infrasound wavefronts. Event position, satellite position, dawn and dusk, and $\pm 50°$ magnetic latitudes are indicated, respectively, by a red circle, a white triangle, yellow and blue dashed lines, and black and red dashed lines. The two lower panels present, respectively, the air density perturbation (in %) and the vertical acceleration (in m/s^2) as function of time after the earthquake (in minutes) along GOCE satellite track. Data, SM, and FM synthetics are plotted, respectively, as gray thick line, black thin line, and black thick line. FM synthetics are divided by 2.

3. Post-Seismic Infrasound Propagation

[9] The propagation of seismic waves at the surface of the Earth generates infrasounds in the atmosphere. Most of these acoustic waves are refracted back to the surface within the lower atmosphere waveguide. Only the infrasonic waves propagating at almost vertical incidence (smaller than 6°) are able to reach the altitude of GOCE ($\approx$ 270 km). Below 100–200 km of altitude, these waves are amplified due to the conservation of kinetic energy in a medium of decreasing density. The atmosphere viscosity and thermal conductivity then controls the attenuation of these infrasounds in the thermosphere, acting like a low-pass filter for which the corner frequency decreases with altitude [*Artru et al.*, 2004].

[10] The seismic coupling between the solid earth and its atmosphere is modeled in this study by two different approaches. First, a simple model (SM) of infrasound propagation is computed assuming that the waves propagate from the ground to the GOCE altitude as vertically propagating plane waves excited by the ground displacement at the surface [*Garcia et al.*, 2005]. The ground displacement due to the quake is modeled by gravito-acoustic normal mode summation up to 155 mHz [*Zhao and Dahlen*, 1993, 1995] within ak135 spherical Earth's model [*Kennett et al.*, 1995]. Then the acoustic wave propagation time, amplification, and attenuation from the ground to GOCE altitude are computed with the NRLMSISE-00 atmosphere model [*Picone et al.*, 2002] below each GOCE measurement. This simple modeling does not take into account the atmosphere to solid coupling feedback and the complex wave propagation in the atmosphere. However, the low level of atmosphere to solid feedback and the almost vertical propagation justify such a simple wave propagation model. Its ability to take into account lateral variations of sound speed and attenuation in the atmosphere by using different atmospheric models for each measurement point is an advantage.

[11] A second post-seismic infrasound modeling, denoted full model (FM), is performed through a variational normal mode computation of the full solid/atmosphere Earth [*Lognonné et al.*, 1998; *Artru et al.*, 2001]. In this case, the infrasound waves are described more correctly, with the exception of ion-neutral collision processes. However, the modeling of wave propagation is limited to radial mod-

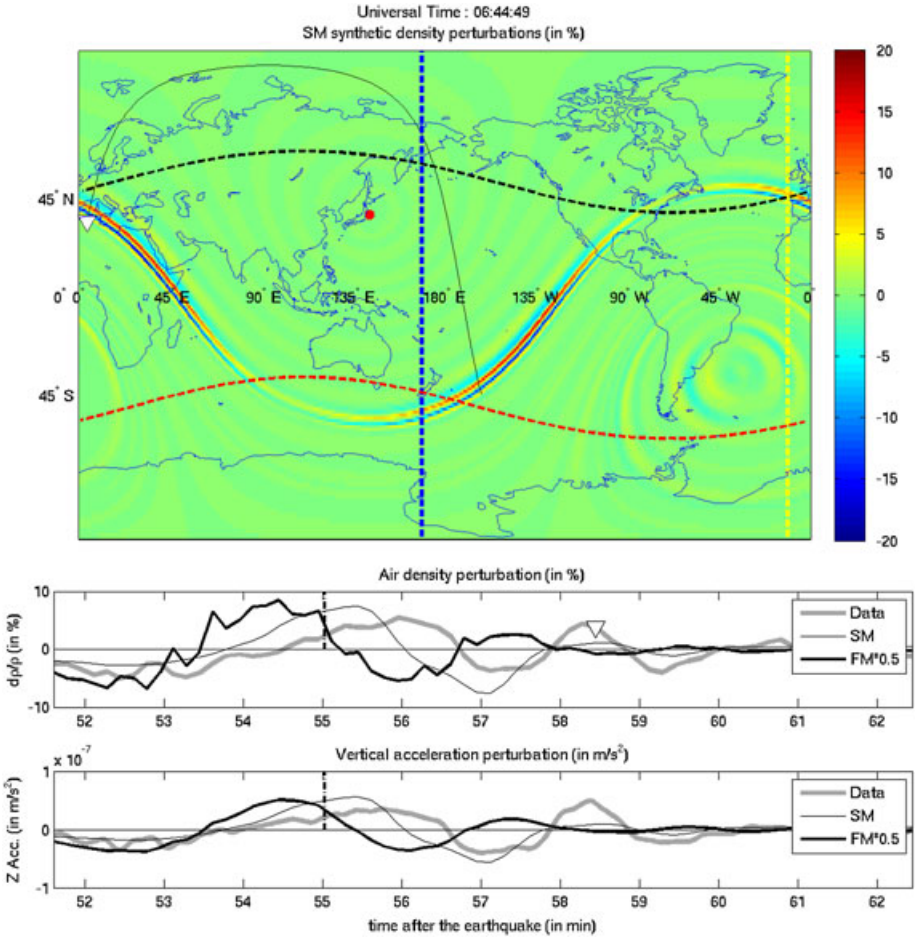

Figure 3. Same legend as Figure 2, for signals corresponding to a doubling of the post-seismic infrasound wavefront.

els of solid and atmosphere parts, excluding lateral variations. Models PREM [*Dziewonski and Anderson*, 1981] and NRLMSISE-00 at epicenter space/time location are chosen, respectively, for the solid Earth and the atmosphere. The seismic source parameters for SM and FM are the ones provided by Global CMT project [*Dziewonski et al.*, 1981].

[12] Our simulations allow to compute the wind and density perturbations of the atmosphere due to infrasounds. From FM, the post-seismic infrasonic waves at the altitude of GOCE present dominant periods larger than 60 s and vertical velocities up to 100 m/s which is about 10 times larger than horizontal ones. The perturbation of the vertical acceleration of the satellite is induced by both a change in lift force due to density variations and a variation of the wind angle of attack on the spacecraft due to the added infrasonic vertical wind. The perturbation of GOCE vertical acceleration (ΔA_z) is deduced from synthetic perturbations of atmosphere density ($\Delta\rho$) and vertical wind velocity (ΔV_z) by the simple aerodynamic formula:

$$\Delta A_z = \frac{1}{M}\left(\frac{1}{2}\Delta\rho C_z A_{ref} V^2 + F\sin\alpha\right) \quad (1)$$

where M is the spacecraft mass, C_z the lift coefficient, A_{ref} a reference area, V the aerodynamic velocity, and F is the thruster force. All these parameters are extracted from GOCE mission data sets. Assuming that vertical winds are only due to the infrasounds, we obtain $\sin\alpha = \frac{\Delta V_z}{V_h}$, where V_h is the horizontal spacecraft velocity and α is the wind attack angle. The second term dominates the lift force variation by a factor five.

4. Results and Discussion

[13] Figures 2 and 3 present the data geometry and the comparison between data and model outputs for the two signals described above.

[14] The first high-frequency signal observed in GOCE data is identified as a crossing of the infrasound wavefront by the satellite over the Pacific. The high frequencies observed ($\approx$ 14 mHz) are due to a large differential velocity between post-seismic infrasound head waves of $\approx$ 800 km wavelength propagating horizontally at the speed of seismic surface waves ($\approx$ 4 km/s) and the GOCE satellite (7.8 km/s). Infrasonic waves generated by vertical ground displacements due to both SV seismic wave (26.5 min after the quake) and Rayleigh surface waves (main signal) are observed in GOCE records. Both propagation models reproduce the amplitudes within a factor 2. However, only the FM predicts the correct start and end of times of the perturbation waveform due to proper modeling of atmospheric wave propagation. A time shift of –10 s and +10 s are observed,

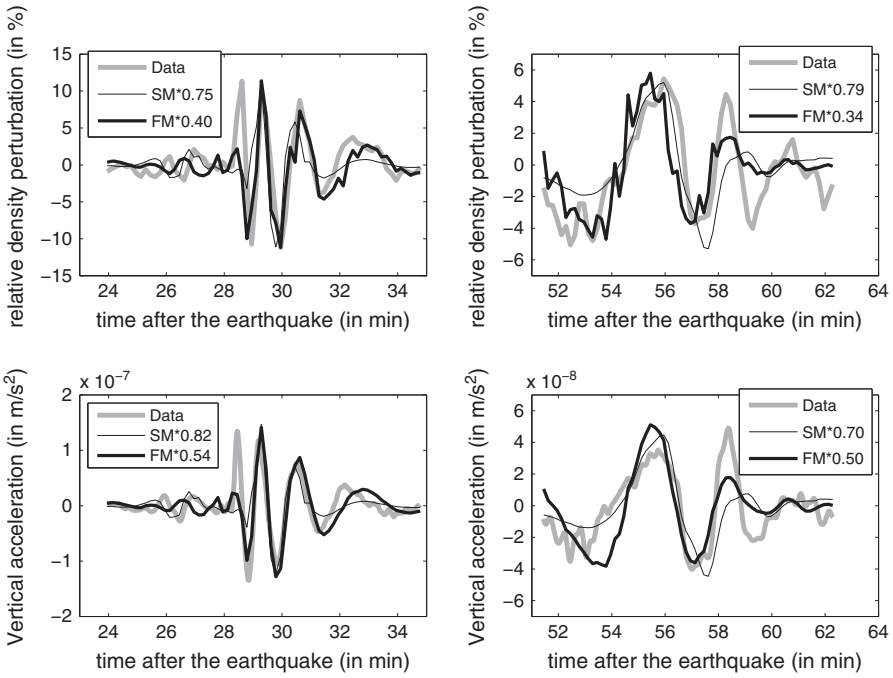

Figure 4. Comparison between data and synthetic waveforms for relative density perturbations (top) and vertical accelerations (bottom) during first (left frames) and second (right frames) crossings of the infrasound wavefront. Data, SM, and FM synthetics are plotted, respectively, as gray thick line, black thin line, and black thick line. Time shifts of synthetic waveforms are identical for density and vertical acceleration. SM and FM synthetics are shifted, respectively, by 10 s and –10 s for the first crossing, and +30 s and +60 s for the second crossing. Amplitude scaling factors are indicated in the legend.

respectively, for SM and FM between data and synthetic waveforms.

[15] The second signal is identified as a doubling by GOCE of the infrasound wavefront following the Rayleigh surface waves. The frequencies observed in GOCE data ($\approx$ 6 mHz) are lower than that for the first signal due to a lower relative velocity ($\approx$ 4 km/s) between the infrasonic waves and the spacecraft. The air density perturbation waveform, amplitude, and shape are well modeled by SM, but FM synthetic is delayed by about 60 s, which is about 2% of the travel time of the seismic surface wave. Such faster long period surface waves are expected along a polar great circle [*Beucler and Montagner*, 2006] and suggest the importance of an improved modeling taking into account lateral variations. The time shifts due to atmospheric sound velocity variations and to atmospheric winds were estimated, respectively, smaller than 15 and 5 s from NRL-MSISE00 and HWM93 [*Hedin et al.*, 1996] empirical models. Nevertheless, we cannot exclude that both sound velocity profile and thermospheric winds can differ significantly from values predicted by empirical models.

[16] Figure 4 compares the synthetic waveforms to data after amplitude scaling and alignment. As expected, SM simulations are able to reproduce only the main part of the signal, whereas FM almost exactly matches the observed waveforms. In particular, a similar frequency content is observed between FM synthetics and data for both infrasound crossing events. Moreover, the similar frequency content of vertical acceleration data (sampled at 1 Hz) and density perturbation data (sampled at 0.1 Hz) suggests that no aliasing is observed, even when the relative velocity is high ($\approx$ 12 km/s). This strongly constrains the frequency content of infrasonic waves and consequently the atmosphere viscosity and the thermal conductivity through atmospheric attenuation models of acoustic waves.

[17] It is interesting to notice that both data and synthetic acoustic waves present a ratio between vertical acceleration and air density perturbations larger than the one observed for the gravity waves in the polar areas. This is due to the high vertical velocities compared to horizontal ones in the post-seismic infrasounds. So, the combination of these two data should help to discriminate between post-seismic infrasounds and internal gravity waves.

[18] Analysis of the GOCE data for other large earthquakes was unsuccessful because wavefront crossings happened in the polar zone (Sumatra events on 11 April 2012) or because of a lack of data (Chile event on 27 February 2010). For the other events, our simulations demonstrate that the signal is too small to be recovered by GOCE. Analyses of GRACE (480 km altitude) and CHAMP (320 km altitude) databases were also unsuccessful because the infrasonic waves are strongly attenuated before arriving at the altitude of these two gravimetric satellites. Our estimate of the optimum altitude for such a detection is around 300 km, in between the GOCE and the CHAMP spacecraft altitudes.

5. Conclusions

[19] The air density and vertical acceleration perturbations measured by GOCE along its track just after the Tohoku earthquake have been clearly identified as perturbations induced by the propagation of post-seismic infrasonic waves. Our model is able to reproduce amplitudes and waveforms, but precise timing is controlled by lateral variations of solid and atmospheric elastic wave speeds, which are not

included in our model. The waveform fit validates our propagation and attenuation models. High vertical acceleration to air density perturbation ratio is predicted and observed for such post-seismic infrasonic waves, allowing discrimination with internal gravity waves.

[20] These data open a new way to directly probe post-seismic infrasounds through low Earth orbit satellites like GOCE. They also constitute a benchmark for post-seismic infrasound modeling because the neutral acoustic wave is probed directly and not through electron density perturbations, airglow emissions, or integrated values of these quantities. This validation of our modeling tools allows to gain confidence in our ability to predict the timing and the amplitude of signals expected for other seismic events, in preparation of future space based observations.

[21] However, the influence of atmospheric winds and 3-D seismic and sound velocity variations should be included in future modeling tools. Moreover, the GOCE data set remains to be explored more deeply to search for other infrasounds or gravity waves related to tectonic activity, including those related to the tsunamis.

[22] **Acknowledgments.** We thank Li Zhao for providing Earth's normal modes, computed in ak135 Earth's model up to 155 mHz, which were used to compute SM synthetics. We also thank Sharon Kedar and an anonymous reviewer for their constructive reviews. This study was funded by CNES through space research scientific projects and by ESA.

References

Arai, N., M. Iwakuni, S. Watada, Y. Imanishi, T. Murayama, and M. Nogami (2011), Atmospheric boundary waves excited by the tsunami generation related to the 2011 great Tohoku-Oki earthquake, *Geophys. Res. Lett.*, *38*, L00G18, doi:10.1029/2011GL049146.

Artru, J., P. Lognonné, and E. Blanc (2001), Normal modes modelling of post-seimic ionospheric oscillations, *Geophys. Res. Lett.*, *28*, 697–700.

Artru, J., T. Farges, and P. Lognonné (2004), Acoustic waves generated from seismic surface waves: Propagation properties determined from doppler sounding observation and normal-modes modeling, *Geophys. J. Int.*, *158*, 1067–1077.

Beucler, É., and J.-P. Montagner (2006), Computation of Large Anisotropic Seismic Heterogeneities (CLASH), *Geophys. J. Int.*, *165*, 447–468, doi: 10.1111/j.1365-246X.2005.02813.X.

Bruinsma, S. L., and M. Fedrizzi (2012), Simultaneous observations of TADs in GOCE, CHAMP and GRACE density data compared with CTIPe, *AGU Fall Meeting Abstr.*, 2012, SA33B-05.

Chum, J., F. Hruska, J. Zednik, and J. Lastovicka (2012), Ionospheric disturbances (infrasound waves) over the Czech Republic excited by the 2011 Tohoku earthquake, *J. Geophys. Res.*, *117*(A16), A08319, doi: 10.1029/2012JA017767.

Dautermann, T., E. Calais, and G. S. Mattioli (2009), Global Positioning System detection and energy estimation of the ionospheric wave caused by the 13 July 2003 explosion of the Soufrière Hills Volcano, Montserrat, *J. Geophys. Res*, *114*, B02202, doi:10.1029/2008JB005722.

Doornbos, E., J. van den IJssel, H. Luehr, M. Foerster, and G. Koppenwallner (2010), Neutral density and crosswind determination from arbitrarily oriented multiaxis accelerometers on satellites, *J. Spacecraft Rockets*, *47*, 580–589, doi:10.2514/1.48114.

Drinkwater, M. R., R. Floberghagen, R. Haagmans, D. Muzi, and A. Popescu (2003), GOCE: ESA's First Earth Explorer Core Mission, *Space Sci. Rev.*, *108*, 419–432, doi:10.1023/A:1026104216284.

Dziewonski, A., and D. Anderson (1981), Preliminary reference Earth model, *Phys. Earth Planet. Inter*, *25*, 297–356.

Dziewonski, A., T.-A. Chou, and J. Woodhouse (1981), Determination of earthquake source parameters from waveform data for studies of global and regional seismicity, *J. Geophys. Res.*, *86*, 2825–2852.

Floberghagen, R., M. Fehringer, D. Lamarre, D. Muzi, B. Frommknecht, C. Steiger, J. Piñeiro, and A. da Costa (2011), Mission design, operation and exploitation of the gravity field and steady-state ocean circulation explorer mission, *J. Geodesy*, *85*, 749–758, doi:10.1007/s00190-011-0498-3.

Galvan, D. A., A. Komjathy, M. P. Hickey, P. Stephens, J. Snively, Y. Tony Song, M. D. Butala, and A. J. Mannucci (2012), Ionospheric signatures of Tohoku-Oki tsunami of March 11, 2011: Model comparisons near the epicenter, *Radio Science*, *47*, RS4003, doi:10.1029/2012RS005023.

Garcia, R., P. Lognonné, and X. Bonnin (2005), Detecting atmospheric perturbations produced by Venus quakes, *Geophys. Res. Lett.*, *32*, L16,205.

Hedin, A. E., E. L. Fleming, A. H. Manson, F. J. Schmidlin, S. K. Avery, R. R. Clark, S. J. Franke, G. J. Fraser, T. Tsuda, F. Vial, and R. A. Vincent (1996), Empirical wind model for the upper, middle and lower atmosphere, *J. Atmos. Terr. Phys.*, *58*, 1421–1447.

Hines, C. O. (1960), Internal atmospheric gravity waves at ionospheric heights, *Can. J. Phys.*, *38*, 1441, doi:10.1139/p60-150.

Kennett, B., E. Engdahl, and R. Buland (1995), Constraints on seismic velocities in the Earth from traveltimes, *122*, 108–124.

Kherani, E. A., P. Lognonné, N. Kamath, F. Crespon, and R. Garcia (2009), Response of the ionosphere to the seismic triggered acoustic waves: electron density and electromagnetic fluctuations, *Geophys. J. Int.*, *176*, 1–13, doi:10.1111/j.1365-246X.2008.03818.X.

Kherani, E. A., P. Lognonné, H. Hébert, L. Rolland, E. Astafyeval, G. Occhipinti, P. Coïsson, D. Walwer, and E. R. de Paula (2012), Modelling of the total electronic content and magnetic field anomalies generated by the 2011 Tohoku-Oki tsunami and associated acoustic-gravity waves, *Geophys. J. Int*, *191*, 1049–1066, doi:10.1111/j.1365-246X.2012.05617.X.

Kobayashi, N. (2007), A new method to calculate normal modes, *Geophys. J. Int*, *168*, 315–331, doi:10.1111/j.1365-246X.2006.03220.X.

Lognonné, P., E. Clévédé, and H. Kanamori (1998), Normal mode summation of seismograms and barograms in a spherical earth with realistic atmosphere, *Geophys. J. Int*, *135*, 388–406.

Makela, J. J., P. Lognonné, H. Hébert, T. Gehrels, L. Rolland, S. Allgeyer, A. Kherani, G. Occhipinti, E. Astafyeva, P. Coïsson, A. Loevenbruck, E. Clévédé, M. C. Kelley, and J. Lamouroux (2011), Imaging and modeling the ionospheric airglow response over Hawaii to the tsunami generated by the Tohoku earthquake of 11 March 2011, *Geophys. Res. Lett.*, *38*, L00G02, doi:10.1029/2011GL047860.

Maruyama, T., T. Tsugawa, H. Kato, A. Saito, Y. Otsuka, and M. Nishioka (2011), Ionospheric multiple stratifications and irregularities induced by the 2011 off the Pacific coast of Tohoku Earthquake, *Earth, Planets and Space*, *63*, 869–873, doi:10.5047/eps.2011.06.008.

Nishitani, N., T. Ogawa, Y. Otsuka, K. Hosokawa, and T. Hori (2011), Propagation of large amplitude ionospheric disturbances with velocity dispersion observed by the SuperDARN Hokkaido radar after the 2011 off the Pacific coast of Tohoku Earthquake, *Earth, Planets and Space*, *63*, 891–896, doi:10.5047/eps.2011.07.003.

Occhipinti, G., P. Coïsson, J. J. Makela, S. Allgeyer, A. Kherani, H. Hébert, and P. Lognonné (2011), Three-dimensional numerical modeling of tsunami-related internal gravity waves in the Hawaiian atmosphere, *Earth, Planets and Space*, *63*, 847–851, doi: 10.5047/eps.2011.06.051.

Picone, J. M., A. E. Hedin, D. P. Drob, and A. C. Aikin (2002), NRLMSISE-00 empirical model of the atmosphere: Statistical comparisons and scientific issues, *J. Geophys. Res*, *107*, 1468, doi:10.1029/2002JA009430.

Raveloson, A., R. Kind, X. Yuan, and L. Ceranna (2012), Locating the Tohoku-Oki 2011 tsunami source using acoustic-gravity waves, *J. Seismol.*, *16*, 215–219, doi:10.1007/s10950-011-9262-7.

Rolland, L. M., P. Lognonné, and H. Munekane (2011a), Detection and modeling of Rayleigh wave induced patterns in the ionosphere, *J. Geophys. Res.*, *116*(A15), A05320, doi:10.1029/2010JA016060.

Rolland, L. M., P. Lognonné, E. Astafyeva, E. Alam Kherani, N. Kobayashi, M. Mann, and H. Munekane (2011b), The resonant response of the ionosphere imaged after the 2011 off the Pacific coast of Tohoku Earthquake, *Earth, Planets and Space*, *63*, 853–857, doi: 10.5047/eps.2011.06.020.

Watada, S., and H. Kanamori (2010), Acoustic resonant oscillations between the atmosphere and the solid earth during the 1991 Mt. Pinatubo eruption, *J. Geophys. Res.*, *115*(B14), B12319, doi:10.1029/2010JB007747.

Zhao, L., and F. A. Dahlen (1993), Asymptotic eigenfrequencies of the Earth's normal modes, *Geophys. J. Int.*, *115*, 729–758, doi:10.1111/j.1365-246X.1993.tb01490.X.

Zhao, L., and F. A. Dahlen (1995), Asymptotic normal modes of the Earth—II. Eigenfunctions, *Geophys. J. Int.*, *121*, 585–626, doi:10.1111/j.1365-246X.1995.tb05736.X.